Vulnerability analysis of steel roofing cladding

Ji, X.; Huang, Guilan; Zhang, X.; Kopp, Gregory

DOI:
10.1016/j.engstruct.2017.11.068

Document Version
Peer reviewed version

Citation for published version (Harvard):
Ji, X, Huang, G, Zhang, X & Kopp, G 2018, 'Vulnerability analysis of steel roofing cladding: influence of wind directionality', *Engineering Structures*, vol. 156, pp. 587-597. https://doi.org/10.1016/j.engstruct.2017.11.068

Vulnerability analysis of steel roofing cladding: influence of wind directionality

Xiaowen Ji, Guoqing Huang, Xinxin Zhang, Gregory A. Kopp

Xiaowen Ji: S. M. ASCE; PhD Student, School of Civil Engineering, Southwest Jiaotong University, Chengdu, China 610031, jixiaowen900308@gmail.com

Guoqing Huang (corresponding author): Professor, School of Civil Engineering, Southwest Jiaotong University, Chengdu, China 610031, ghuang1001@gmail.com

Xinxin Zhang: Engineer, Berkshire Hathaway Specialty Insurance, Boston, MA, USA 02110, Xinxin.Zhang@bhspecialty.com

Gregory A. Kopp: M. ASCE; Professor, Boundary Layer Wind Tunnel Laboratory, Faculty of Engineering, University of Western Ontario, London, ON, Canada N6A5B9, gakopp@uwo.ca

Abstract

Steel roofing is widely used for non-residential facilities. However, it is vulnerable to high winds. This paper addresses a damage estimation framework that incorporates wind loading correlation and wind directionality effects for steel roofing. In this framework, external pressures were measured from wind tunnel testing. At positions where pressure measurements are not available, a proper orthogonal decomposition (POD) method is introduced to interpolate external wind pressures. Internal pressures due to openings in the building envelope are taken into account by simulation. Then, the internal forces on fasteners distributed on the steel roof are evaluated by the influence surface method, with corresponding peak values estimated by a Gumbel conversion approach. Furthermore, the failure probability of a single

cladding element and the damage ratio for the whole roof are determined based on Monte Carlo simulation (MCS), where the correlation among internal forces of fasteners is incorporated by a Nataf transformation. Finally, wind directionality effects are integrated in order to provide a comprehensive damage assessment for the roofing. Although the proposed framework works for existing buildings, it may potentially benefit the performance-based design for new low-rise buildings.

Keywords: Wind damage estimation; Steel roofing; Proper orthogonal decomposition; Internal pressure; Correlation; Nataf transformation; Wind directionality

1. Introduction

Metal structures are widely used for low-rise buildings, especially for non-residential buildings. Based on the statistics from Metal Building Manufacturers Association (MBMA), approximately 65% of non-residential low-rise buildings are built with metal structures in USA (e.g., Dabral and Ewing 2009). Among these metal structures, lightweight steel structures represent a significant proportion and are popular for warehouses, sheds, airplane hangars and industrial buildings, which are vulnerable during hurricanes (or typhoons or tropical cyclones), thunderstorms and tornadoes (e.g., Perry et al. 1990; Ginger et al. 2007). For example, typhoon "Rananim" in 2004 devastated industrial buildings in Zhejiang Province, China, including collapsed area of 2.72 million m^2 and damaged area of 7.56 million m^2 (Song and Ou 2009).

Post-event damage surveys have indicated that the majority of damage to steel

45 structures is related to the breach of the envelope instead of the collapse of the main
46 frame (NIST 2006). The breach of the roofing not only introduces losses to the
47 building itself, but also triggers further damage to interior contents due to secondary
48 perils, e.g., rain penetration. Additionally, business interruption increases indirect
49 losses of income, which is a common concern for the insurance sector. Therefore, it is
50 important to analyze and predict wind-induced damage for steel roofing in order to
51 conduct damage mitigation and risk management assessments.

52 Damage analysis of low-rise buildings, especially wood-frame structures, under
53 high winds has received significant attentions from the engineering community. Lee
54 and Rosowsky (2005) assessed the wind-induced fragility of roof sheathing for light
55 wood-frame structures. Li and Ellingwood (2006) proposed probabilistic risk
56 assessment methods to evaluate performance and reliability of low-rise light-frame
57 wood residential constructions in hurricane-prone region of the United States, where
58 the importance of uncertainties is highlighted. Recently, aerodynamic databases have
59 been applied to wind damage assessments. Zhao and Gu (2011) presented a database-
60 assisted wind vulnerability assessment model for metal buildings. Huang et al. (2015)
61 introduced a database-assisted probabilistic damage estimation approach for asphalt
62 shingle roofing. Konthesingha et al. (2015) developed a vulnerability model for metal-
63 clad industrial building in a tropical cyclone region. Huang et al. (2016) developed a
64 damage estimation method for roof panels where the wind loading correlation was
65 taken into account. In addition to structural component damage analyses, the wind-
66 induced economic loss for metal roofing was discussed by Dabral and Ewing (2009).

Despite these achievements, there is a need to develop an integrated database-assisted approach to incorporate important factors such as wind loading correlation and wind directionality effects for the wind-induced damage analysis of low-rise building roof components. Cope et al. (2005) showed that the correlation of the surface pressures varies with direction and became strong under quartering winds and winds perpendicular to the roof gable. Huang et al. (2016) had found that the wind loading correlation may significantly influence the standard deviation (STD) of the damage ratio for roof panels. Although directionality effects have been widely recognized and incorporated in structural and cladding design, it has not yet been well addressed in vulnerability studies. Obviously, the wind damage of roof components will also depend on wind direction. To develop a comprehensive understanding of structural vulnerability, and for the sake of wind-induced damage mitigation and risk management, one needs to integrate the vulnerabilities of all directions with the local wind climate data within a framework that also considers wind load correlations and other influential factors.

Based on an illustrative low-rise building model whose wind pressure data were measured in a wind tunnel study, a wind damage estimation method incorporating the wind loading correlation and wind directionality for steel roofing is addressed in this paper. The paper is organized as follows. First, descriptions of the steel roofing and wind pressure data are introduced. Second, POD is adopted to interpolate the external wind pressure for roof locations where there are no pressure data. Third, the internal pressure is determined by simulation. Fourth, the internal forces on fasteners

89 distributed on the steel roof are computed with the aid of the influence-surface
90 approach, with the corresponding peak internal forces estimated by a Gumbel
91 conversion method. Fifth, the failure probability of a single panel and the damage
92 ratio of whole roof are determined based on MCS, where the correlation among
93 internal forces on fasteners is considered by a Nataf transformation. Sixth, the
94 influence of wind directionality is incorporated in the damage estimation. In the end,
95 concluding remarks are given.

96 **2. Descriptions of wind pressures and steel roofing**

97 The illustrative prototype industrial building used in this study has a full-scale
98 size of 62.5 ft × 40 ft × 12 ft (19.05 m × 12.2 m × 3.66 m), a roof slope of 1:12, and is
99 assumed to be located in suburban terrain. The wind pressure data were obtained from
100 wind tunnel tests conducted at the University of Western Ontario (UWO), as reported
101 by Ho et al. (2005), with significant comparisons to existing data provided by St.
102 Pierre et al. (2005). The model scale was 1:100, with 335 taps distributed on the roof
103 top. These are shown as blue dots in Figure 1. The sampling frequency was 500 Hz
104 with a sampling time of 100 s. The tests were conducted in suburban terrain with
105 roughness length of about 0.3 m, under a reference mean wind speed of 13.7 m/s at
106 the equivalent of 10 m above the ground, which corresponds to a mean wind speed of
107 6.1 m/s at the roof height (3.66 m). The tests were carried out at various wind angles
108 of attack (AOAs) with intervals of 5˚ from 0˚ to 90˚ and from 270˚ to 360˚. In the rest
109 of paper, if without any specification, wind speeds are referred to 10-min mean wind
110 speeds at the roof height.

111 There are many types of steel cladding profiles that are commonly used in
112 construction, such as pierced-fixed and standing-seam steel cladding systems. Due to
113 the requirements of large spans, low price, and simplicity of construction and also
114 being well-researched (e.g., Mahaarachchi and Mahendran 2009), the high-strength
115 trapezoidal steel cladding with closely spaced ribs is selected as the roof panel for this
116 study. In the current study, the size of a single cladding panel is assumed to be 750
117 mm × 6096 mm with a thickness of 0.6 mm. The height of crest is 35 mm and ribs are
118 closely spaced with an interval of 125 mm between two neighboring crests. The
119 layout of the cladding on the roof is shown in Figure 1 where 50 (2 × 25) steel
120 cladding panels are distributed on the roof. The cladding is made of high-strength
121 steel G550 (yielding stress = 690 MPa). Self-tapping screws with head diameters of
122 11 mm are assumed as the connection fasteners. Further details on this type of
123 cladding can be found in Mahaarachchi and Mahendran (2009).

124 For the cladding cross section, four screws are used to connect the roof cladding
125 to the purlins at alternate crests. Along the rib, four screws are also uniformly
126 distributed. A schematic description can be found in Figures 2 (a) and (b). The
127 locations of screws on a cladding panel are represented by the coordinate system
128 shown in Figure 2 (a). For example, x2y3 denotes the screw at the intersection of line
129 x2 and line y3 on the panel. Two adjacent cladding panels overlap at marginal crests
130 and share common screws, as shown in Figure 2 (c). The purlin spacing of the
131 prototype building in Mahaarachchi and Mahendran (2009) is between 0.9 m and 1.1
132 m. And in practice, the purlin spacing at the edge of the building is smaller to resist

larger wind pressures. For convenient illustration, the spacing has been adjusted to reduce the number of screws here.

3. POD-based wind pressure interpolations

To determine the wind-induced internal forces on a screw, ideally, the associated cladding panels should be assigned sufficient pressure taps in the wind tunnel experiment. However, not every panel satisfies this requirement, as shown in Figure 1. It can be seen that, for many panels, there are no pressure taps. In order to evaluate the internal forces on the screws, ten proxy taps are evenly assigned along the central line of the each of the panels (see the red "+" in Figure 1). The pressures at these locations are interpolated from existing taps. Several interpolation techniques have been developed and applied for various purposes in database-assisted design (DAD), such as POD and artificial neural networks (ANN) (e.g., Tamura et al. 1997; Chen et al. 2002, 2004). Previous studies have shown that POD has good performance for wind-induced pressure interpolation (e.g., Bienkiewicz et al. 1993; Tamura et al. 1997) and extrapolation (Chen et al. 2004). In the present study, POD will be used to reconstruct the wind pressure field on the low-rise building roof due to its adaptability and easy implementation. One advantage of POD is that it can characterize a multivariate process with a few modes.

If one assumes that $\mathbf{C_P}(t) = \{C_{P_1}(t), C_{P_2}(t), \cdots, C_{P_N}(t)\}^T$ is a zero-mean N-variate fluctuating wind pressure coefficient vector, where N is the number of taps in the wind tunnel testing, POD can be used to find a set of optimal orthonormal basis vectors $\mathbf{\Theta} = [\Theta_1, \Theta_2, \cdots, \Theta_N]$ and $\mathbf{C_P}(t)$ can be expanded as

$$\mathbf{C_P}(t) = \mathbf{\Theta a}(t) = \sum_{i=1}^{N} \Theta_i a_i(t) \tag{1}$$

where the component $a_i(t)$ is the projection of $\mathbf{C_P}(t)$ on the basis vector Θ_i, $i = 1, 2, \cdots, N$. Note that the mean component has been removed as discussed by Tamura et al. (1997). The basis vector set $\mathbf{\Theta}$ can be determined from the eigenvalue equation (Bienkiewicz et al. 1993)

$$\mathbf{R_p A\Theta} = \mathbf{\Theta\Lambda} \tag{2}$$

where $\mathbf{R_p}$ is the covariance matrix of $\mathbf{C_P}(t)$; $\mathbf{A} = diag(A_1, A_2, \cdots, A_N)$ and A_i is the tributary area of the i th pressure tap; $\mathbf{\Lambda} = diag(\lambda_1, \lambda_2, \cdots, \lambda_N)$ is diagonal matrix and λ_i is the i th eigenvalue. If the pressure taps are distributed uniformly and tributary areas associated with different taps are identical, then Eq. (2) is rewritten as

$$\mathbf{R_p\Theta} = \mathbf{\Theta\Lambda}^{\#} \tag{3}$$

where $\mathbf{\Lambda}^{\#} = diag(\frac{\lambda_1}{A}, \frac{\lambda_2}{A}, \cdots, \frac{\lambda_N}{A})$ and A is the tributary area. If the pressure taps are distributed non-uniformly, Eq. (2) can be pre-multiplied by $\mathbf{A}^{1/2}$ and an equivalent form is given as (Jeong et al. 2000)

$$\mathbf{R_P^*\Theta^*} = \mathbf{\Theta^*\Lambda} \tag{4}$$

where $\mathbf{R_P^*} = \mathbf{A}^{1/2}\mathbf{R_P A}^{1/2}$ and $\mathbf{\Theta^*} = \mathbf{A}^{1/2}\mathbf{\Theta}$. Note that the modification guarantees that the transformed $\mathbf{R_P^*}$ is a real and symmetric matrix, and allows the Cholesky decomposition. The target orthogonal basis vector then can be obtained through the inverse transformation

$$\mathbf{\Theta} = \mathbf{A}^{-1/2}\mathbf{\Theta^*} \tag{5}$$

It is clear that the eigenvalue matrix $\mathbf{\Lambda}$ is unchanged in the transformation.

176 Once the value of the basis vector for the proxy tap is estimated by the spatial
177 interpolation, the fluctuation of the wind pressure at this tap can be interpolated from
178 non-uniformly distributed taps. In this study, the first 300 modes are applied to
179 reconstruct the wind pressure time histories. The interpolated fluctuation of the wind
180 pressure coefficient at an existing tap (highlighted by a circle in Figure 2) is compared
181 with the measured counterpart in Figure 3. Consistency can be found in time histories
182 and lower frequency part of power spectral densities (PSDs). Similar results can be
183 found for other taps. Figure 4 shows the interpolated fluctuating pressure coefficient
184 at a proxy tap (highlighted by a rectangle in Figure 1). By the spatial interpolation, the
185 mean component of the wind pressure coefficients at the proxy taps is obtained.

186 **4. Incorporation of internal pressures**

187 Internal pressure appears because of the leakage or openings of a building in
188 response to external wind pressures. Because internal pressure has a significant
189 influence on the structural cladding system, it has been investigated by many scholars
190 (e.g., Holmes 1979; Oh et al. 2007). Previous studies showed that internal pressure is
191 affected by various factors, such as local external pressure, opening size, building
192 volume and flexibility of building envelope (e.g., Oh et al. 2007). Based on the work
193 by Holmes (1979), Oh et al. (2007) showed that simulation of internal pressure time
194 histories for buildings with a dominant opening and/or small leakage in the walls can
195 be accurately simulated using external wind pressures, such as those from the
196 database of Ho et al. (2005), as input.

197 Clearly, internal pressures are dependent on the damage state of the building

198 envelope and cladding. In reality, the wind-induced damage on the building envelope
199 and cladding is a progressive process and the determination of internal pressure is
200 challenging in that additional wind tunnel experiments are usually required. To
201 simplify the damage process, in this study, buildings under high winds are assumed to
202 undergo the following three stages. Stage 1: Enclosed building. In the beginning, the
203 building is nominally sealed with background leakage. In this case, the internal
204 pressure is usually negative (i.e., suction) and increases the load on the windward wall
205 and reduces the wind load on the roof. Stage 2: Partially-enclosed building. The wall,
206 especially a door or window, may be broken due to wind-borne debris-impacts or
207 larger net pressure loads. Loss of these components causes a dominant opening on the
208 wall and makes the building partially enclosed. At this stage, the internal pressure
209 usually becomes positive, which leads to an increase of the net wind loads on the roof
210 and makes roof cladding more vulnerable to wind. Stage 3: Roof cladding loss or
211 component failures. At this stage, portions of the roof panels may be removed,
212 causing new openings on the roof. Accordingly, the internal pressure may decrease, to
213 some extent. Because the roof cladding tends to be most vulnerable at the second
214 stage, partially-enclosed buildings are studied herein. The related internal pressure can
215 be obtained by either wind tunnel tests (such as the UWO data) or via simulation, with
216 similar accuracy (Oh et al. 2007). In this study, the latter will be adopted. In addition,
217 the internal pressure in the third stage is assumed to be unchanged, which may be
218 conservative for the cladding damage estimation. Although the wind damage of a
219 building is also sensitive to its construction and the cladding system details, this study

220 focuses on the damage to the roof system conditioned on a given construction and
221 cladding system.

222 For a single opening in the wall, the governing equation for determining the
223 internal pressure within the building volume is obtained from the unsteady form of the
224 Bernoulli equation (for a recent derivation, see Oh and Kopp 2014). This equation,
225 which represents the conservation of energy of the flow through the opening, is (e.g.,
226 Holmes 1979; Holmes and Ginger 2012):

227 $$\frac{\rho l_e V}{\gamma a P_0}\ddot{C}_{pi}+\left[\frac{\rho V \bar{U}_h}{2\kappa\gamma a P_0}\right]^2 \dot{C}_{pi}\left|\dot{C}_{pi}\right|+C_{pi}=C_{pe} \qquad (6)$$

228 where ρ is the air density; l_e is the effective length of an "air slug"; V is the internal
229 volume; γ is the ratio of specific heat capacities of air; a is the opening area; P_0 is the
230 atmospheric pressure; $\bar{U}_h$ is the mean wind speed at reference height; κ is the
231 discharge coefficient compensating for various energy losses; C_{pe} and C_{pi} denote the
232 external and internal pressure coefficient, respectively. According to Vickery and
233 Bloxham (1992), in the present study, $l_e=\sqrt{a\pi}/2$ and $\kappa=0.6$ will be adopted. It
234 should be mentioned that the effects of friction losses are not incorporated here.
235 However, it must be considered for narrow and long openings. Because Eq. (6) has
236 the form of a spring-mass-damper system, the internal pressure has a natural
237 frequency that is known as the Helmholtz frequency, $\frac{1}{2\pi}\sqrt{\frac{\kappa\gamma a P_0}{\rho l_e V}}$, which is the
238 resonant frequency of the internal pressures (e.g., Holmes 1979; Oh et al. 2007).

239 Similar to Oh et al. (2007), a rectangular dominant opening is assumed on front
240 wall under AOA of 270° (see Figure 1). The ratio of the opening area to the wall area

241 is assumed to be 3.2%, while the building porosity is considered to be negligibly
242 small for the current study. While the current study is illustrative, neglecting the
243 leakage should be reasonable for the damage estimation when one considers the other
244 uncertainties. A 4th-order Runge-Kutta method can be used to solve the above
245 nonlinear differential equation. Note that the opening is assumed to appear on front
246 wall instead of side walls. That is, for AOAs from 180˚-360˚, the opening is same to
247 that for AOA of 270˚, and for AOAs from 0˚-180˚, it is symmetrical to that for AOA
248 of 270˚.

249 For mean wind speed of 37 m/s and AOA of 315˚, the simulated internal pressure
250 C_{pi} is presented together with a corresponding external pressure C_{pe} in Figure 5 (a).
251 Here, 37 m/s is used for illustrative purposes and is representative of a magnitude
252 where damage may be observed. It can be seen internal pressures are almost
253 coincident with the external wall pressures for this particular case with the amplitude
254 of the internal pressures being slightly larger than that of the external pressure due to
255 the Helmholtz resonance. PSD functions are also given in Figure 5 (b). The peak in
256 PSD of C_{pi} is the Helmholtz frequency, which is 2.4 Hz in full scale. Together with
257 (interpolated) external pressures on the roof, the simulated internal pressure will be
258 used to estimate the net wind load on the cladding.

259 **5. Determination of internal forces and their peaks on screws**

260 High winds can cause large uplift forces on roof cladding, and these forces will
261 be transferred to the self-tapping screw fasteners. As a consequence, dimpling around
262 a screw arises initially and cracks appear. Eventually, the steel cladding will be pulled

263 through the screw connection (i.e., pull-through failure). It should be noted that for
264 cladding systems on metal buildings, failures due to low-cycle fatigue (e.g.,
265 Mahendran 1990; Xu 1995, 1997; Henderson and Ginger 2011) are not considered in
266 the current methodology and analysis; rather, failures mainly due to stress
267 concentrations or internal forces in the screws are considered in the development of
268 the method. In this section, an influence-surface-based approach is used to calculate
269 internal (i.e., tension due to uplift) forces on screws, firstly. Then the peak value
270 distributions are estimated via a Gumbel conversion method.

271 To estimate the internal forces on screws, a direct way is to perform the finite
272 element (FE) analysis for all claddings and screws. However, such an analysis needs
273 significant computational time. According to Mahaarachchi and Mahendran (2009),
274 the internal forces of screws on any cladding panel can be estimated individually on a
275 single- or half-cladding-panel basis. In this study, to improve the calculation
276 efficiency, the (linear) influence coefficient approach is used to estimate the internal
277 forces on a screw (e.g., Henderson 2010; Kopp 2013). Accordingly, the internal force
278 of a screw can be obtained as follows

279 $$X(t) = \iint q(x, y, t) I_c(x, y) dxdy \tag{7}$$

280 where $I_c(x, y)$ is the internal-force, influence coefficient at position (x, y); $q(x, y, t)$
281 is the corresponding net pressure (summation of the external and internal pressures).
282 Because the layout of screws is the same for all cladding sheets and each cladding
283 sheet is bi-symmetric, only the internal force influence coefficients for 4 screws are
284 needed. For illustration, an influence surface for the internal force on screw x2y3 is

given in Figure 6 where the vertical axis represents the influence coefficient. It reveals that the internal force is mainly due to the pressure near the crest, where the screw is located. Compared with the aforementioned, direct approach, the influence-surface-based approach is efficient for the determination of internal forces on screws.

Usually, the duration of a pressure time history of wind pressure from a wind tunnel is 20 to 60 min in full scale. The same length is applied to the internal forces on the screw. Hence, the traditional block maximum method is not applicable in the evaluation of the probability density function (PDF) of the peak internal force during the interval of 10 min or 1 h. However, if the peak value distribution of the sample approaches the Gumbel distribution, a Gumbel conversion method, which was introduced by Cook and Mayne (1980), can project Gumbel parameters for a given longer interval based on those determined from a shorter interval. Numerous experimental results have validated the appropriateness of the Gumbel distribution in modeling the peak wind pressure (e.g., Cook and Mayne 1980; Holmes and Cochran 2003). Peng et al. (2014) applied this method to project Gumbel parameters for a 15-min duration using those determined from 15 segments of 1-min duration and illustrated that the conversion method performed well for wind pressure peak prediction. The conversion method is appropriate to estimate PDFs of peak internal forces for hundreds of screws due to its relative simplicity, accuracy and efficiency.

Let W_{T_1} denote the peak value of the internal force process over T_1 min, say, 1 min. Suppose W_{T_1} follows Gumbel distribution, i.e.,

$$\Psi_{W_{T_1}}(w) = \exp\{-\exp[-\alpha_{w_{T_1}}(w - \hat{w}_{T_1})]\} \tag{8}$$

where the mode $\widehat{w}_{T_1}$ is the most likely value and $1/\alpha_{w_{T_1}}$ is the dispersion. If the cumulative distribution function (CDF) of the peak value W over T min, say, 10 min or 1 h, is given as

$$\Psi_W(w) = \exp\{-\exp[-\alpha_w(w-\widehat{w})]\} \tag{9}$$

If peak values from different subsamples over T_1 min are mutually independent, then the peak value distribution over T min can be computed as (e.g., Cook and Mayne 1980; Huang 2008)

$$\Psi_W(w) = [\Psi_{W_{T_1}}(w)]^{T/T_1} = \exp\{-\exp[-\alpha_{w_{T_1}}(w-\widehat{w}_{T_1}) + \ln(T/T_1)]\} \tag{10}$$

The mode and dispersion parameters are given as

$$\widehat{w} = \widehat{w}_{T_1} + \ln(T/T_1)/\alpha_{w_{T_1}};\ \alpha_w = \alpha_{w_{T_1}} \tag{11}$$

The product $\Pi_w = \alpha_w \widehat{w}$ is a dimensionless characteristic product.

In this paper, the internal force time history is divided into subsamples with intervals of 1 min, under various mean wind speeds. For instance, the number of subsamples is about 27, for a wind speed of 37 m/s. Although T_1 = 1 min has been used for wind pressure data by Peng et al. (2014) and Gavanski et al. (2016), the independence of peak internal forces over 1 min shall be examined here. The internal force at screw x2y2 on Cladding A under AOA of 315° is selected as the example. Under the mean wind speed equal to 25, 37 and 49 m/s at roof height, the associated autocorrelation functions are shown in Figure 7 where the time lag is in the full-scale dimensions. It can be seen that the autocorrelation coefficients drop below 0.2 after 5, 3 and 2.5 s under mean wind speeds of 25, 37 and 49 m/s, respectively. This is a good indication of independence between any two peak values separated by more than 5

329 seconds. Similar results can be found for other screws. Hence, peak values of internal
330 forces over 1 min can be reasonably assumed to be independent. Under such an
331 assumption, peak values from subsamples are fitted by Gumbel distribution. Then, the
332 CDF of peak values over 1 min is converted to that over 10 min via Eqs. (10) and
333 (11).

334 **6. Consideration of correlation for peak internal forces**

335 Cope et al. (2005) illustrated that the high correlations of the surface pressures
336 are induced by quartering winds and winds perpendicular to the roof gable.
337 Subsequently, highly correlated wind pressures may lead to high correlations among
338 internal forces on screws. Huang et al. (2016) showed that highly correlated pressures
339 could cause larger variation of the damage ratio, or higher risk for roof components.
340 Hence, the correlation among the peak internal forces should be considered for
341 estimates of the wind-induced damage on steel cladding. However, it is difficult to
342 determine the correlation for peak values over 10 min directly using the current UWO
343 data, which is of limited length (around 20~40 min in the full scale).

344 To make the proposed framework feasible, an alternative to approximately
345 estimate the correlation for peak internal forces over 10 min will be introduced. In this
346 alternative, the relationship for the correlations of peak internal forces over 1 min and
347 10 min is assumed to be equivalent to that for peak wind pressures, which will be
348 estimated from a set of very long wind pressure data. The derivation is presented in
349 the Appendix. Then, the correlation for peak values over 10 min can be approximately
350 estimated from that for peak values over 1 min. To incorporate the correlation among

peak internal forces in the cladding damage estimation, the Nataf transformation is adopted (e.g., Liu and Der Kiureghian 1986), which relates correlated non-Gaussian variables to correlated Gaussian counterparts.

Assume a random variable vector with components made up of the peak internal forces on screws such that $\mathbf{W} = \left[W_1, W_2, \cdots, W_n\right]^T$ whose marginal CDF is $F_{W_j}\left(w_j\right)$, $j = 1, 2, \cdots, n$ and n is the number of screws. This vector can be transformed to its corresponding standard Gaussian random vector $\mathbf{Z} = \left[Z_1, Z_2, \cdots, Z_n\right]^T$ by

$$Z_j = \Phi^{-1}[F_{W_j}\left(w_j\right)], \; j = 1, 2, \cdots, n \tag{12}$$

where $\Phi(\cdot)$ denotes the standard Gaussian CDF. The Nataf transformation can be derived as (e.g., Huang et al. 2016)

$$f_{\mathbf{W}}(\boldsymbol{w}) = f_{W_1}(w_1) f_{W_2}(w_2) \cdots f_{W_n}(w_n) \frac{\varphi_n(\mathbf{z}, \mathbf{R}_\mathbf{Z})}{\varphi(z_1)\varphi(z_2)\cdots\varphi(z_n)} \tag{13}$$

where $f_{\mathbf{W}}(\boldsymbol{w})$ is the joint PDF of peak internal forces and $\varphi_n(\mathbf{z}, \mathbf{R}_\mathbf{Z})$ is the standard Gaussian n-variate joint PDF with the correlation matrix $\mathbf{R}_\mathbf{Z}$.

With known ρ_{jk}^w, the correlation coefficient between W_j and W_k, can be expressed as

$$\rho_{jk}^w = \int_{-\infty}^{\infty}\int_{-\infty}^{\infty}\left(\frac{w_j - \mu_j}{\sigma_j}\right)\left(\frac{w_k - \mu_k}{\sigma_k}\right)\varphi_2(z_j, z_k, \rho_{jk}^z)dz_j dz_k \tag{14}$$

where μ_j and σ_j are the mean and STD of W_j, respectively; and ρ_{jk}^z (correlation coefficient between Z_j and Z_k) is an element in $\mathbf{R}_\mathbf{Z}$. An important lemma is that ρ_{jk}^w is a strictly monotonic function with respect to ρ_{jk}^z (Liu and Der Kiureghian, 1986). This leads to one-to-one mapping between ρ_{jk}^w and ρ_{jk}^z. To avoid iteration in above

372 equation, a series of empirical formulae were fitted by Liu and Der Kiureghian
373 (1986). If W_j and W_k both follow Gumbel distribution, Eq. (14) can be approximated
374 as

375 $$\rho_{jk}^{z} = 1.064\rho_{jk}^{w} - 0.069(\rho_{jk}^{w})^2 + 0.005(\rho_{jk}^{w})^3 \quad (15)$$

376 Obviously, both the marginal CDF and correlation of the non-Gaussian variables are
377 maintained under the Nataf transformation.

378 **7. Damage estimation of steel roofing**

379 **7.1 Failure probability and damage ratio of a roof cladding**

380 Based on a comprehensive parametric study for the pull-through failures of the
381 trapezoidal steel cladding at the screw connections, Mahaarachchi and Mahendran
382 (2009) developed strength formulae for trapezoidal steed claddings with closed space
383 ribs. When G550 steel is used, the mean of the strength *R* is given as

384 $$\mu_R = 0.04 \times \left(4.7 - \frac{20 f_y d_h}{Et}\right)^2 \left(\frac{h_c}{h_p}\right)^{3/4} \left(\frac{W_t}{W_c}\right)^{1/5} \left(12 + \frac{1500t^2}{Ld_h}\right)^{1/3} d_h t f_y \quad (16)$$

385 where the steel yield stress $f_y = 690$ MPa; the diameter of screw head $d_h = 11$ mm;
386 the Young's modulus $E = 200$ GPa; the cladding crest height $h_c = 35$ mm; the crest
387 pitch $h_p = 125$ mm; the cladding trough width $W_t = 81.5$ mm; the cladding crest
388 width $W_c = 43.5$ mm; the cladding thickness $t = 0.6$ mm and the span between
389 purlins $L = 1981.2$ mm. The coefficient of variation (the ratio of the STD to the
390 mean) is 0.12. The cladding strength *R* is assumed to follow Gaussian distribution, in
391 the current case, with mean of 2.15 kN and STD of 0.26.

392 Once the peak internal force on the screw is larger than the cladding strength
393 around the screw, the cladding may suffer from the pull-through failure. Due to the

394 lack of the research and experimental data, the peak internal force and the cladding
395 strength around a screw are regarded to be independent. The failure probability of
396 cladding around a screw is given by

397 $$s = \iint_{r \le w} f_R(r) f_W(w) dr dw \tag{17}$$

398 where $f_R(r)$ is PDF of the cladding strength around the screw.

399 Previous investigations showed that 90% wind load would be redistributed to
400 two adjacent screws on the same crest if a screw fails to take the load (Henderson
401 2010; Konthesingha et al. 2015). As a consequence, internal forces on these two
402 screws will significantly increase, and the redistributed internal force may exceed the
403 cladding strength and the corresponding cladding sheet will very likely undergo
404 failure. Hence, it is appropriate to assume that the failure of one of the screws on a
405 cladding panel leads to the failure of the whole panel.

406 Apparently, the failure probability of a cladding panel is determined by the peak
407 internal forces and resistances at the screws on that cladding. The failure probability
408 can be expressed as

409 $$p = 1 - \iint_{w_1 < r_1} \iint_{w_2 < r_2} \cdots \iint_{w_{n_s} < r_{n_s}} f_{\mathbf{R}}(\boldsymbol{r}) f_{\mathbf{W}}(\boldsymbol{w}) d\boldsymbol{r} d\boldsymbol{w} \tag{18}$$

410 where $f_{\mathbf{R}}(\boldsymbol{r})$ is the joint Gaussian PDF of strengths and can be determined based on
411 the assumption of independence. Note that $f_{\mathbf{W}}(\boldsymbol{w})$, which is defined in section 6, has
412 incorporated the correlation among peak internal forces. In this study, the number of
413 screws, n_s, is 8 due to the symmetric layout of screws.

414 Suppose the number of cladding panels over the entire roof is N_C. To estimate

415 the overall damage of claddings over the roof, the damage ratio is used. It describes
416 the extent of damage on the roof cladding and is defined as the percentage of total
417 failed panels, i.e.,

418 $$D = M_C / N_C \tag{19}$$

419 where M_C is the failed cladding number, and M_C and D are random variables.

420 **7.2 Monte Carlo simulation**

421 It is time-consuming to evaluate Eqs. (18) and (19) by a numerical method
422 because they depend on several parameters including peak internal forces and
423 strengths around screws, and their correlations. MCS is more efficient than a
424 numerical method in estimating the damage ratio over the entire roof as well as the
425 failure probability for each single cladding. It should be noted that the internal forces
426 on many pairs of screws will be fully correlated. For example, the internal forces on
427 screws x2y2 and x2y3 on a cladding are identical. One of two fully correlated forces
428 in the simulation is taken out and the simulated force can be adopted for both.

429 Assume MCS is repeated for n_t rounds. In the m th simulation, the correlated
430 peak internal forces at all screws are simulated via the Nataf transformation, firstly.
431 The peak internal forces at all screws can be simulated in the following way. The
432 correlated Gaussian vector $\mathbf{Z}$ is simulated according to

433 $$\mathbf{R_Z} = \mathbf{L}\mathbf{L}^T;\ \mathbf{Z} = \mathbf{L}^{-1}\mathbf{U} \tag{20}$$

434 where $\mathbf{U}$ is the independent standard Gaussian vector and the lower triangular matrix
435 $\mathbf{L}$ shall be obtained by Cholesky decomposition of $\mathbf{R_Z}$. Once the sample of Gaussian
436 vector $\mathbf{Z}$ is generated, that of the non-Gaussian vector $\mathbf{W}$ can be simulated

accordingly. Further details can be found in Huang et al. (2016).

In addition, Cholesky decomposition for matrix $\mathbf{R_Z}$ may be not applicable because negative eigenvalues may still exist. These negative values appear due to highly correlated forces on different screws and/or computational errors. To solve this difficulty, the $\mathbf{R_Z}$ matrix should be manipulated. First, this matrix can be written as

$$\mathbf{R_Z} = \mathbf{V}^T \mathbf{\Omega} \mathbf{V} \tag{21}$$

where $\mathbf{V}$ is the eigenvector matrix and $\mathbf{\Omega}$ is the diagonal eigenvalue matrix. The negative eigenvalue in matrix $\mathbf{\Omega}$ can be replaced by a small positive value such as 0.001 in order to make the Cholesky decomposition available. Results show that the simulation is not sensitive to the minor changes in the eigenvalues. After the correlated peak internal forces have simulated, the independent resistances associated with those internal forces are generated accordingly. Note that the correlation of resistances is neglected due to a lack of available data.

Let $f_{l,m}$ denote whether the l th cladding has failed in the m th simulation such that $f_{l,m} = 0$ or 1 for undamaged or damaged, respectively. The failure probability of the l th cladding is

$$p_l = \frac{1}{n_t} \sum_{m=1}^{n_t} f_{l,m} \tag{22}$$

where $\sum_{m=1}^{n_t} f_{l,m}$ is the number of the failure for the l th cladding in the simulations. The damage ratio for m th simulation is given by

$$d_m = \frac{1}{N_C} \sum_{l=1}^{N_C} f_{l,m} \tag{23}$$

where $\sum_{l=1}^{N_C} f_{l,m}$ is the number of failed cladding panels in the m th simulation. According to discussions by Huang et al. (2016), the random variable D will approach the Gaussian distribution approximately. The mean and STD of damage ratio are determined as

$$\mu_D = \frac{1}{n_t}\sum_{m=1}^{n_t} d_m \; ; \; \sigma_D = \sqrt{\frac{1}{n_t}\sum_{m=1}^{n_t}(d_m - \mu_D)^2} \tag{24}$$

7.3 Results and discussions

In the following discussions, the correlation for peak values over 10 min will be denoted as C_{10min}. For comparison, another three types of correlations will be also used to investigate the influence of the correlation of peak internal forces: the correlation for the parent process (denoted by C_{par}), the correlation for peak values over 1 min (denoted by C_{1min}), and no correlation (denoted by C_0). Note that C_{par} and C_{1min} are estimated based on the limited data, and C_{10min} is approximately estimated from C_{1min}.

Table 1 shows the correlation coefficients for internal forces on selected screws under mean wind speed of 37 m/s at roof height and AOA of 315° (The corresponding cladding numbers are marked in Figure 1). It can be observed that the correlation coefficients decrease from C_{par} to C_{1min} and further C_{10min}, which is consistent with the results in Luo and Huang (2016). Also, strong correlations can be found even for the distant screws. For example, the correlation coefficients between x2y2 on Cladding A and x2y3 on Cladding D are estimated as 0.917, 0.877 and 0.760 for C_{par}, C_{1min} and C_{10min}, respectively.

In total, 10,000 rounds of simulations are conducted based on C_{par}, C_{1min}, C_{10min} and C_0, respectively. Once the peak internal forces and resistances at all screws are simulated, the failures for all screws can be judged and corresponding failure probabilities can then be estimated by the simulation. Failure probabilities can be evaluated numerically from Eq. (17). It should be pointed out that the correlation of peak internal force has no influence on screw failures. The contour map for the failure probabilities of all 608 screws under the mean wind speed of 37 m/s at roof height and AOA of 315˚ is shown in Figure 8. It can be seen that screws close to the leading edges are more vulnerable. It is also seen that screws along the line x2 (e.g., x2y3) on a cladding panel have larger failure probabilities, which indicates cladding failure possibly starts from these positions. This is attributed to the facts that these screws have relatively larger tributary areas and suffer from relatively larger wind loading.

Subsequently, failure probabilities of all cladding panels can be obtained. From Eq. (18), the correlation of peak internal forces will affect these probabilities. Results show that C_{par}, C_{1min}, C_{10min} and C_0 have little effect on the failure probability of a cladding. With C_{10min} for illustration, failure probabilities of all cladding under mean wind speeds of 33, 37 and 41 m/s and AOAs of 270˚, 315˚ and 360˚ are shown in Figure 9. Here, the progressive damage can be observed. With the increase of the mean wind speed, the breach will spread from the windward side to leeward side under AOA of 270˚, and start from the windward corner and spread radially to the leeward corner under 315˚, and gradually extend from one edge to another one under 360˚. It can also be seen that the roof faces the highest risk for 270˚; not for 315˚. This

observation can be explained as follows. Typically, the roof damage associated with AOA of 315° is expected to be largest due to the existence of the conical vortex if only the external pressures are considered. However, when a breakage on a windward wall is assumed, the internal pressure has a significant influence on the roof damage. In current study, the internal pressure under AOA of 270° on Stage 2 makes the roof most vulnerable.

The means and STDs of the damage ratios for C_{par}, C_{1min}, C_{10min} and C_0 under various mean wind speeds and AOAs are plotted in Figure 10. Results show that the correlation has a negligible effect on the mean damage ratio. This is similar to results reported by Huang et al. (2016), where the wind loading correlation has no effect on the mean damage ratio for the roof panels. However, the STD may be sensitive to the correlation, i.e., it becomes larger with the increase of the correlation. For example, under mean wind speed of 37 m/s and AOA of 315°, the STDs of the damage ratio are about 0.147, 0.141 and 0.132 for C_{par}, C_{1min} and C_{10min}, and that for C_0 drops to less than 0.045. This is attributed to the fact that higher correlations among internal forces on screws cause the failures at different cladding panels more likely. Especially, if the wind loading correlations approach unit, those claddings may either fail or survive together, which will greatly increase the variation of damage ratio. Figure 11 shows the CDFs of the damage ratios for C_{par}, C_{1min}, C_{10min} and C_0 under mean wind speed of 37 m/s and AOA of 315. It can be seen that the CDFs for first three correlations are almost identical, indicating correlations for parent process of internal forces, peak internal forces over 1 min and 10 min have similar effects on the distribution of

damage ratio. Besides, the consideration of correlation (e.g., C_{par}, C_{1min} and C_{10min}) may increase the variation of damage ratio, which may lead to the building in higher risks.

8. Directionality in damage estimation

The evaluation of directionality effect is critically important because of the coupling of building orientation and directional wind distribution. A given structure and its components respond differently to the wind of the same magnitude but different AOAs given all other conditions being equal. Also, wind speed distributions are different in each distribution due to the nature of macro- and micro-meteorological effects, e.g., effects from large scale wind climate and local terrain features. The ignorance of such effect would result in inaccurate predictions. While the effect of wind directionality on probabilistic estimation of wind load effects of structures has drawn significant attentions for load design purpose (e.g., Simiu and Scanlan 1996; Laboy-Rodrigues et al 2014; Zhang and Chen 2015), its study in vulnerability analysis has been limited in the literature. For example, ASCE 7-10 specifies a directionality reduction factor of 0.85 for the structural design of roofs and claddings (ASCE 2010). However, the directionality effect on vulnerability, i.e., damage status of a building altered by the directionality effect of the actual building aerodynamics (determined via the wind tunnel study), has rarely been considered as a separate parameter in previous literatures.

The consideration of directionality effects is also important since the wind climate for a prescribed location is unique and will introduce directionality, i.e., there

may be a dominant direction for winds in terms of both the frequency and magnitude. The overall vulnerability for a particular building at a particular location should be an integration of the vulnerabilities conditioned on prescribed directions, over all directions. Thus, the following discussions focus on a fully probabilistic method that considers the wind directionality, directional wind speed correlations as well as uncertainties in the damage ratio within a unified framework.

In this study, the historical wind speed record from Baltimore International Airport was used. The record was extracted from Automated Surface Observation System (ASOS) database operated by National Oceanic and Atmospheric Administration (NOAA) (ftp://ftp.ncdc.noaa.gov/pub/data/asos-onemin/). The original 2-min mean wind speeds at 10-m height were converted to 10-min mean wind speed at the roof height of the building adopted in this paper. Wind speeds covering 360 degrees are categorized into eight representative sectors with each denoted by their central directions α_i = 45°, 90°, ⋯, 360° (i = 1, 2, ⋯, 8 indicates directions NE, E, ⋯, N, respectively, as shown in Figure 12). Monthly maximum wind speed data are selected in each sector. In total, 156 monthly (from 2000 Jan to 2013 Dec) maxima are collected for every sector. In the following discussion, the damage analysis of steel cladding is performed with the consideration of the wind loading correlation among the screw peak forces over 10 min (i.e., C_{10min}).

8.1 Without consideration of variation of damage ratio

Denote the joint CDF of directional extreme wind speeds as $H(v_1, v_2, \cdots, v_{n_d})$ where n_d is the total number of directions being partitioned. Such joint CDF can be

derived from the multivariate extreme value theory using a Gaussian Copula model, which is expressed as (Zhang and Chen 2015; Luo and Huang 2016)

$$H(v_1, v_2, \cdots, v_{n_d}) = G_{n_d}(\Phi^{-1}[\Psi_{V_1}(v_1)], \Phi^{-1}[\Psi_{V_2}(v_2)], \cdots, \Phi^{-1}[\Psi_{V_{n_d}}(v_{n_d})]) \quad (25)$$

where Φ^{-1} is the inversed CDF of standard Gaussian distribution; G_{n_d} is the CDF of n_d-dimensional normal distribution with the zero mean and the covariance matrix $\boldsymbol{\Sigma}$ in which $\Sigma_{ii} = 1$ and $\Sigma_{ij} = \Sigma_{ji} = E\left[\Phi^{-1}[\Psi_{V_i}(v_i)], \Phi^{-1}[\Psi_{V_j}(v_j)]\right]$; and $\Psi_{V_i}(v_i)$ ($i = 1, 2, \cdots, n_d$) is the CDF of annual maximum wind speed in the i th direction. It is proper to adopt the Gumbel distribution in Eq. (9) to model the annual maximum wind speed in any direction. Hence, the CDF of the annual maximum can be determined from that of monthly maximum following Eq. (11). It should be noted that the Gaussian copula is equivalent to the Nataf transformation: both relate the non-Gaussian variables to the Gaussian counterparts and can be united under the well-known multivariate Gaussian translation theory (Grigoriu 2007). The extreme wind speeds for 50 and 500 -year return period in each direction are plotted in Figure 12. It can be observed that N and NW are two dominant directions in terms of the magnitude of the extreme wind speed.

In engineering practice and in the insurance industry, the mean damage ratio is often of primary concern. The mean damage ratio for a component such as steel roofing can be treated as a function of the mean wind speed from the i th direction. Alternatively, the mean wind speed v_i^d, producing a given damage level d in that direction, can be obtained from Figure 10 (a). Therefore, for a component subjected to wind loads from all directions, the probability not exceeding the damage level d can

588 then be calculated as

589 $$P(D \le d) = H(v_1^d, v_2^d, \cdots, v_{n_d}^d) \quad (26)$$

590 If the directional extreme wind speeds can be assumed to be mutually independent,

591 the estimation by Eq. (26) can be replaced by

592 $$P(D \le d) = \prod_{i=1}^{n_d} \Psi_{V_i}(v_i^d) \quad (27)$$

593 The damage of the steel roofing for Y-year return period, d_Y, can then be determined

594 from

595 $$Y = 1/[1 - P(D \le d_Y)] \quad (28)$$

596 The probabilities for various damage levels are illustrated in Figure 13, where the

597 roofing damages considering wind directionality and those in 8 directions are

598 included. It can be seen NW direction (7 th) retains the dominance among 8 directions

599 due to the larger extreme wind speed and the higher damage risk in this direction. In

600 contrast, another dominant N direction (8 th) has less influence in terms of extreme

601 wind speed due to the lower damage risk. Besides, the consideration of wind

602 directionality effect produces a larger damage estimation compared with those in 8

603 individual directions. This is attributed to the fact that

604 $H(v_1^d, v_2^d, \cdots, v_{n_d}^d) \le \min[\Psi_{V_i}(v_i^d)]$. Furthermore, the directional extreme wind speeds

605 are shown to be mutually independent, as seen in the almost identical estimations by

606 Eqs. (26) and (27). This can be attributed to a dominant NW direction and low

607 correlations among extreme wind speeds across different directions.

608 The aforementioned approach provides the estimation of the roofing damage

609 where the variation of the damage ratio is not considered. If the mean damage ratio is

610 treated as a principle index in damage estimation, this approach will be quite
611 convenient to deal with the wind directionality. Otherwise, the variations of damage
612 ratio should be incorporated, which is discussed in the next subsection.

613 **8.2 With consideration of variation of damage ratio**

614 According to Huang et al. (2016), the STD of the damage ratio is larger when the
615 wind loading has a stronger correlation. This variation around the mean damage ratio
616 causes additional risk, which is sometimes termed as "secondary uncertainty".
617 Ignoring the influence of the secondary uncertainty may result in an inadequate
618 assessment of the risk. The following discussions address the issue of quantifying the
619 damage considering the variation of damage ratio.

620 The probability of D not exceeding damage level d in all directions can be
621 expressed as

622 $$P(D \le d) = \int \cdots \int F_{D_1, D_2, \cdots, D_{n_d}}(d \,|v_1, d\,|v_2, \cdots, d\,|v_{n_d}) h(v_1, v_2, \cdots, v_{n_d}) dv_1 dv_2 \cdots dv_{n_d} \quad (29)$$

623 where $F_{D_1, D_2, \cdots, D_{n_d}}(d_1 |v_1, d_2 |v_2, \cdots, d_{n_d} |v_{n_d})$ is the joint CDF of damage ratios
624 conditioned on extreme wind speed v_i ($i = 1, 2, \cdots, n_d$). If the roofing damage is
625 mutually independent across directions, Eq. (29) becomes

626 $$P(D \le d) = \int \cdots \int \prod_{i=1}^{n_d} F_{D_i}(d\,|v_i) h(v_1, v_2, \cdots, v_{n_d}) dv_1 dv_2 \cdots dv_{n_d} \quad (30)$$

627 where $F_{D_i}(d\,|v_i)$ is the CDF of damage ratio in i th direction under v_i, which is served
628 as a complimentary fragility and obeys exceeding lognormal distribution (Lee and
629 Rosowsky 2005). If the directional extreme wind speeds are mutually independent,
630 which is the particular case for present study, the above formula can be approximated
631 by

$$P(D \le d) = \prod_{i=1}^{n_d} \int F_{D|i,v}(d) \psi_{V_i}(v) dv \tag{31}$$

where $\psi_{V_i}(v)$ is the PDF of extreme wind speed in the i th direction.

Numerical results show that damage ratios across directions are almost independent, which can be explained by the fact that both the peak force and resistance on a fastener are independent for different directions. Hence, Eq. (31) can be used to estimate the damage. The result considering the damage ratio variation is plotted in Figure 13. It is clearly seen that this yields an estimation of a higher damage level in a certain return period (e.g., 50-year). That is, the consideration of damage variation leads to a larger risk for roofing claddings.

9. Conclusions

The paper presents an integrated damage estimation method for steel roofing cladding in high winds. In this method, both the wind loading correlation and wind directionality effects are incorporated. For illustration, the high-strength trapezoidal steel cladding is chosen as the roof sheathing which is connected to building frame by screws. The wind loading is derived from the wind pressure data from a wind tunnel. Some observations and conclusions are given as follows. (1) POD is a useful tool to interpolate wind pressure for the position where the pressure tap is not assigned in the wind tunnel test. (2) The internal pressure can be satisfactorily simulated by current methods. (3) The internal force on the fastener can be computed efficiently by the influence-surface method and its peak value can be estimated conveniently via Gumbel conversion method. (4) The failure probability and damage ratio can be estimated by Nataf transformation -based MCS accurately when the wind loading

correlation is considered. Results show that the wind loading correlation may noticeably increase the variation of the cladding damage. (5) The wind directionality is incorporated into damage estimations in this study. Methods for consideration of mean damage ratio and the variation of damage ratio are developed. Results show that the wind directionality may lead to a larger damage risk for claddings in high winds and its consideration will provide a reliability-consistent solution in risk management.

Moreover, the presented damage estimation framework for the low-rise building roof can be a useful tool in making damage assessments for new or existing buildings. Furthermore, the method may benefit the performance-based design for the low-rise buildings (e.g., Ciampoli et al. 2011).

It should be noted that the proposed framework may not be directly used to other cladding types, like standing-seam clipped cladding. Appropriate modifications should be made to apply this framework, especially in determinations of wind loads on cladding, and the failure mechanisms and influence functions at the connections. Hence, it would be worthwhile to apply the framework to consider different roof types and failure modes in future work.

Appendix Derivation the relation between correlations for peak wind pressures over 1 and 10 min

The very long wind pressure data used to derive the relation between correlations for peak wind pressures over T_1 = 1 min and T = 10 min were obtained from Boundary Layer Wind Tunnel II at UWO. Two 1:50 scale house models, FL27 and FL30, located in the suburban terrain under different AOAs and surroundings were

676 tested. The sampling frequency for model scale is 400 Hz and the sampling time for
677 model scale is 3 h. Based on the assumption that a full-scale mean wind speed at 10 m
678 height in suburban exposure is 31.7 m/s, equivalent to a mean wind speed = 24.2 m/s
679 at the mean roof height of 4 m (The mean roof heights of both houses are roughly 4
680 m), the velocity scale is 1:5, the sampling frequency and time in full scale are 40 Hz
681 and 30 h, respectively. More details can be found in Peng et al. (2014).

682 For each tap, the very long data (30 h) are divided into 1800 segments of 1-min
683 duration and 180 segments of 10-min duration in the following analysis. Correlation
684 coefficients among peak pressure coefficients over 1 min and 10 min are estimated for
685 all test conditions. Because the sampling frequency and time in full scale vary with
686 the different mean wind speed, these variations may influence the correlation of peak
687 values. Thus correlation coefficients under mean wind speeds of 12.1 and 36.3 m/s at
688 the roof height are also investigated. Figure 14 shows the relationship between
689 correlation coefficients over two time intervals for two test conditions (FL27, 120˚,
690 isolated and FL30, 130˚, surrounded) under three different mean wind speeds, where
691 ρ_T and ρ_{T_1} are correlation coefficients for peak values over T and T_1 min. It can be
692 seen that the relationships are similar for different building models, AOAs,
693 surroundings and mean wind speeds.

694 The relationship between correlation coefficients of peak values over 1 min and
695 10 min is fitted by the following polynomial

696 $$\rho_T = \sum_{i=0}^{4} a_i \rho_{T_1}^i \tag{32}$$

697 where the coefficients a_i for i = 0 to 4 are determined as 0.007, 0.241, -0.232, 1.716

and -0.741, respectively. Although the uncertainties in the lower correlation for peak values are large, they should not have the significant effect on the roof damage estimation and can be neglected for simplicity.

Acknowledgments

The support from the National Natural Science Foundation of China (Grant No. 51778546) and Youth Fund Program of Sichuan Province (2016JQ0005) is greatly acknowledged.

Reference

ASCE. (2010). Minimum design loads for buildings and other structures. ASCE7-10, Reston, VA.

Bienkiewicz, B., Ham, H. J., and Sun, Y. (1993). Proper orthogonal decomposition of roof pressure. J. Wind Eng. Ind. Aerodyn., 50, 193-202.

Chen, Y., Kopp, G. A., and Surry, D. (2002). Interpolation of wind-induced pressure time series with an artificial neural network. J. Wind Eng. Ind. Aerodyn., 90(02), 589-615.

Chen, Y., Kopp, G.A., and Surry, D. (2004). Spatial extrapolation of pressure time series on low buildings using proper orthogonal decomposition, Wind Struct., 7, 373-392.

Ciampoli, M., Petrini, F., and Augusti, G. (2011). Performance-based wind engineering: towards a general procedure. Struct. Safety, 33(6), 367-378.

Cook, N. J., and Mayne, J. R. (1980). A refined working approach to the assessment of wind loads for equivalent static design. J. Wind Eng. Ind. Aerodyn., 6(1-2), 125-

720 137.

721 Cope, A. D., Gurley, K. R., Gioffre, M., and Reinhold, T. A. (2005). Low-rise gable
722 roof wind loads: Characterization and stochastic simulation. J. Wind Eng. Ind.
723 Aerodyn., 93(9), 719-738.

724 Dabral, A., and Ewing, B. T. (2009). Analysis of wind-induced economic losses
725 resulting from roof damage to a metal building. J. Business Val. Econ. Loss Anal.,
726 4(2).

727 Gavanski, E., Gurley, K. R., and Kopp, G. A. (2016). Uncertainties in the Estimation
728 of Local Peak Pressures on Low-Rise Buildings by Using the Gumbel Distribution
729 Fitting Approach. J. Struct. Eng., 142(11), 04016106.

730 Ginger, J. D., Henderson, D. J., Leitch, C. J., and Boughton, G. N. (2007). Tropical
731 cyclone larry: estimation of wind field and assessment of building damage. Australian
732 J. Struct. Eng., 7(3), 209-224.

733 Grigoriu, M., (2007). Multivariate distributions with specified marginals:
734 Applications to wind engineering. J. Eng. Mech., 133(2), 174–184.

735 Henderson, D. J. (2010). Response of pierced fixed metal roof cladding to fluctuating
736 wind loads. Ph.D Dissertation, James Cook University.

737 Henderson, D. J., and Ginger, J. D. (2011). Response of pierced fixed corrugated steel
738 roofing systems subjected to wind loads. Eng. Struct., 33(12), 3290-3298.

739 Ho, T. C. E., Surry, D., Morrish, D., and Kopp, G. A. (2005). The UWO contribution
740 to the NIST aerodynamic database for wind loads on low buildings: Part 1. Archiving
741 format and basic aerodynamic data. J. Wind Eng. Ind. Aerodyn., 93(1), 1-30.

742 Holmes, J. D., (1979). Mean and fluctuating internal pressures induced by wind. Proc.
743 5th Intl. Conf. on Wind Eng. 435-440., Fort Collins, Colorado, USA.
744 Holmes, J. D., and Cochran, L. S. (2003). Probability distributions of extreme
745 pressure coefficients. J. Wind Eng. Ind. Aerodyn., 91(7), 893-901.
746 Holmes, J. D., and Ginger, J. D. (2012). Internal pressures – the dominant windward
747 opening case – a review. J. Wind Eng. Ind. Aerodyn., 100(1), 70-76.
748 Huang, G. (2008). Probabilistic analysis of load effects on tall buildings under
749 stationary and nonstationary extreme winds. Ph.D Dissertation, Texas Tech
750 University.
751 Huang, G., He, H., Mehta, K. C., and Liu, X. (2015). Data-based probabilistic damage
752 estimation for asphalt shingle roofing. J. Struct. Eng., 141(12), 04015065.
753 Huang, G., Ji, X., Luo, Y., and Gurley, K. R. (2016). Damage estimation of roof
754 panels considering wind loading correlation. J. Wind Eng. Ind. Aerodyn., 155, 141-
755 148.
756 Jeong, S. H., Bienkiewicz, B., and Ham, H. J. (2000). Proper orthogonal
757 decomposition of building wind pressure specified at non-uniformly distributed
758 pressure taps. J. Wind Eng. Ind. Aerodyn., 87(1), 1-14.
759 Konthesingha, K. M. C., Stewart, M. G., Ryan, P., Ginger, J., and Henderson, D.
760 (2015). Reliability based vulnerability modelling of metal-clad industrial buildings to
761 extreme wind loading for cyclonic regions. J. Wind Eng. Ind. Aerodyn., 147, 176-185.
762 Laboy-Rodríguez, S.T., Gurley, K. R., and Masters, F. J. (2014). Revisiting the
763 directionality factor in ASCE 7. J. Wind Eng. Ind. Aerodyn., 133(4), 225–233.

764 Luo, Y., and Huang, G. (2016). Characterizing dependence of extreme wind
765 pressures. J. Struct. Eng., 10.1061/(ASCE)ST.1943-541X.0001699, 04016208.
766 Kopp, G.A. (2013). Wind Loads on Building Components and Cladding. *Advanced*
767 *Structural Wind Engineering* (ed. Tamura, Y. & Kareem, A.), Springer, Tokyo, 177-
768 195.
769 Lee, K. H., and Rosowsky, D. V. (2005). Fragility assessment for roof sheathing
770 failure in high wind regions. Eng. Struct., 27(6), 857-868.
771 Li, Y., and Ellingwood, B. R. (2006). Hurricane damage to residential construction in
772 the us: importance of uncertainty modeling in risk assessment. Eng. Struct., 28(7),
773 1009-1018.
774 Liu, P. L., and Der Kiureghian, A. (1986). Multivariate distribution models with
775 prescribed marginals and covariances. Prob. Eng. Mech., 1(2), 105-112.
776 Luo, Y, and Huang, G. (2016). "Characterizing dependence of extreme wind
777 pressures." J. Struct. Eng.g (ASCE), 10.1061/(ASCE)ST.1943-541X.0001699,
778 04016208.
779 Mahendran, M. (1990). Fatigue behaviour of corrugated roofing under cyclic wind
780 loading. Civil Engineering Transaction, Institution of Engineers, Australia 32(4), 219-
781 226.
782 Mahaarachchi, D., and Mahendran, M. (2009). Wind uplift strength of trapezoidal
783 steel cladding with closely spaced ribs. J. Wind Eng. Ind. Aerodyn., 97(3), 140-150.
784 NIST (2006). Performance of physical structures in Hurricane Katrina and Hurricane
785 Rita: A reconnaissance report. National Institute of Standards and Technology,

786 Gaithersburg, MD, USA
787 Oh, J. H., Kopp, G. A., and Inculet, D. R. (2007). The UWO contribution to the NIST
788 aerodynamic database for wind loads on low buildings: Part 3. Internal pressures. J.
789 Wind Eng. Ind. Aerodyn., 95(8), 755-779.
790 Oh, J.H. and Kopp, G.A. (2014). Modelling of spatially and temporally-varying cavity
791 pressures in air permeable, double-layer roof systems. Building Environ. 82, 135-150.
792 Peng, X., Yang, L., Gavanski, E., Gurley, K., and Prevatt, D. (2014). A comparison of
793 methods to estimate peak wind loads on buildings. J. Wind Eng. Ind. Aerodyn., 126,
794 11-23.
795 Perry, D. C., Mcdonald, J. R., Saffir, H. S., and Asce, F. (1990). Performance of metal
796 buildings in high winds. J. Wind Eng. Ind. Aerodyn., 36, 985-999.
797 Simiu E., and Scanlan, R. H. (1996). Wind Effects on Structures: Fundamentals and
798 Applications to Design. (Third edition), John Wiley & Sons, NY
799 Song F., and Ou J. (2009). Wind hazard damage estimation of industrial buildings. 7th
800 Asia-Pacific Conf. on Wind Eng., Taipei, Taiwan, China.
801 St. Pierre, L.M., Kopp, G.A., Surry, D., and Ho, T.C.E. (2005). The UWO
802 contribution to the NIST Aerodynamic database for wind loads on low buildings: Part
803 2. Comparison of data with wind load provisions. J. Wind Eng. Ind. Aerodyn., 93(1),
804 31-59.
805 Tamura, Y., Ueda, H., Kikuchi, H., Hibi, K., Suganuma, S., and Bienkiewicz, B.
806 (1997). Proper orthogonal decomposition study of approach wind-building pressure
807 correlation. J. Wind Eng. Ind. Aerodyn., 72, 421-431.

808 Vickery, B. J., and Bloxham, C. (1992). Internal pressure dynamics with a dominant
809 opening. J. Wind Eng. Ind. Aerodyn., 41(1-3), 193-204.
810 Xu, Y. L. (1995). Fatigue performance of screw-fastened light-gauge-steel roofing
811 sheets. J. Struct. Eng., 121(3), 389-398.
812 Xu, Y. L. (1997). Fatigue damage estimation of metal roof cladding subject to wind
813 loading. J. Wind Eng. Ind. Aerodyn., 72(1), 379-388.
814 Zhang, X., and Chen, X. (2015). Assessing probabilistic wind load effects via a
815 multivariate extreme wind speed model: A unified framework to consider
816 directionality and uncertainty. J. Wind Eng. Ind. Aerodyn., 147, 30-42.
817 Zhao, M., and Gu M. (2011). Database-assisted wind vulnerability assessment for
818 metal buildings. Proc. 13th Intl. Conf. on Wind Eng., Amsterdam, Netherlands.

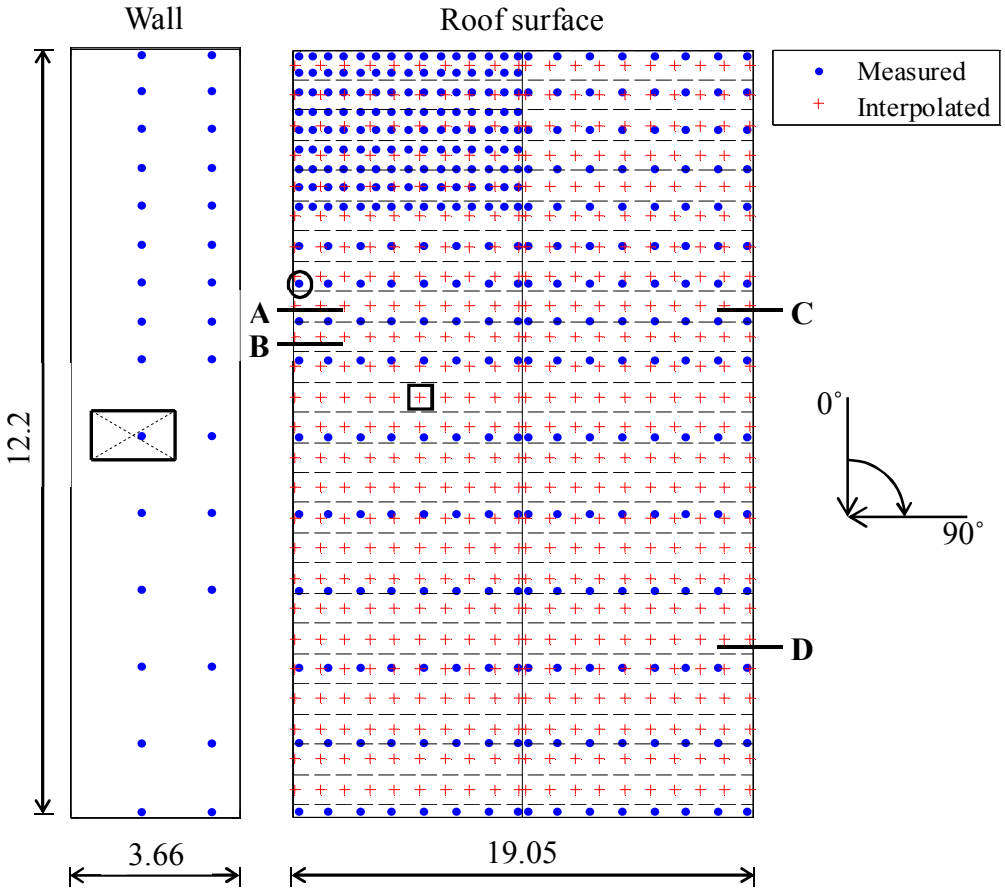

Figure 1 Tap locations and panel layout (Unit: m)

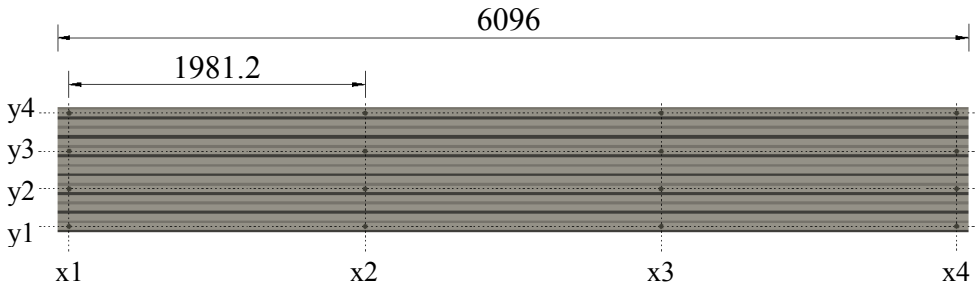

(a) Cladding configuration and screw distribution

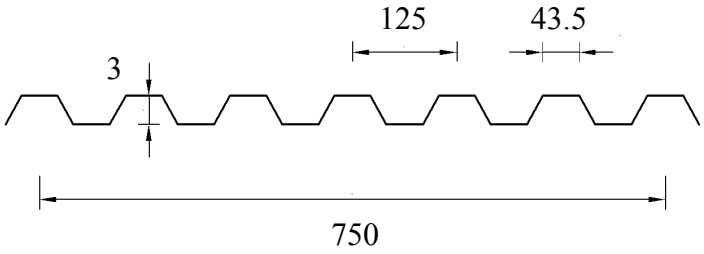

(b) Cross section

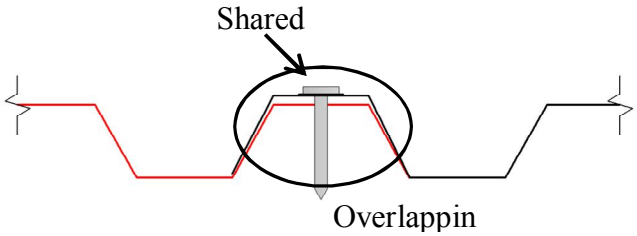

(c) Overlap

Figure 2 Configuration, dimension and joint type of cladding (Unit: mm)

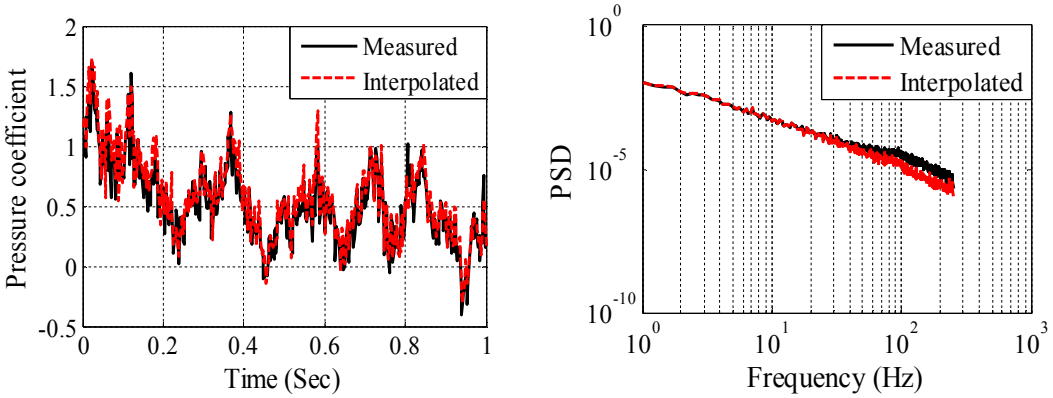

(a) Time histories of fluctuations (b) PSDs of fluctuations

Figure 3 Comparison of measured fluctuation and its interpolated counterpart at an existing tap (AOA of 315°)

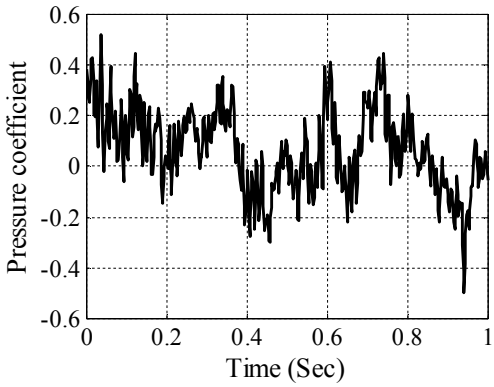

Figure 4 Interpolated fluctuation at a proxy tap (AOA of 315˚)

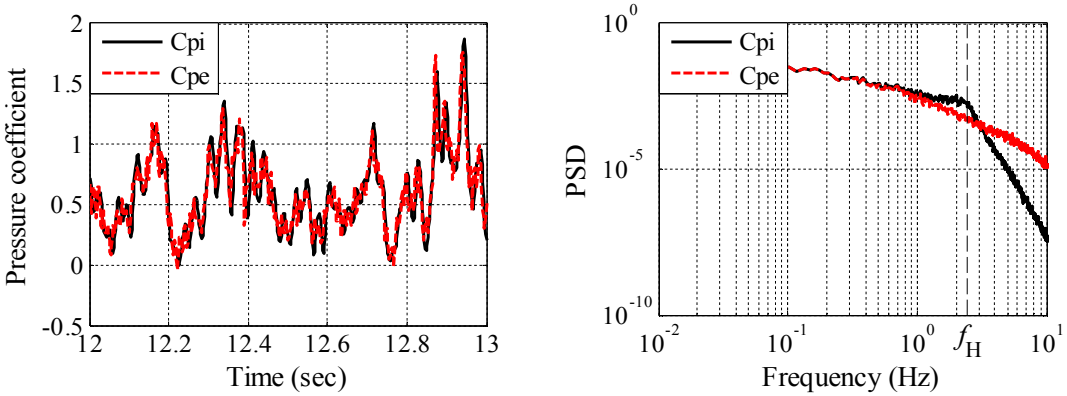

(a) Time series (b) PSD

Figure 5 Time series and spectra of internal and external pressure coefficients under wind speed of 37 m/s and AOA of 315°

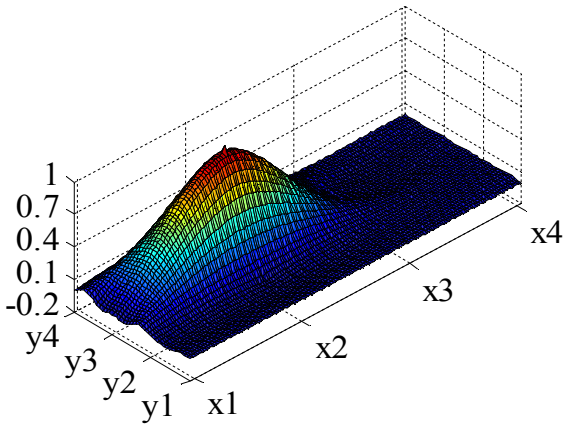

Figure 6 Influence surface for the internal force on screw x2y3

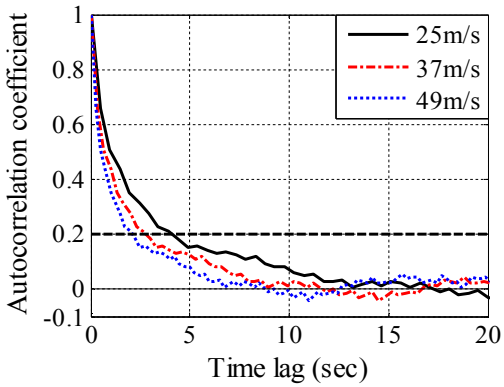

Figure 7 Autocorrelation coefficient of internal force at screw x2y2 on Cladding A

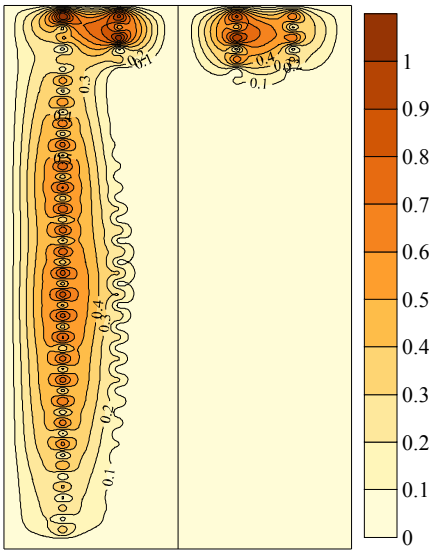

Figure 8 Failure probabilities for screws under speed of 37 m/s and AOA of 315˚

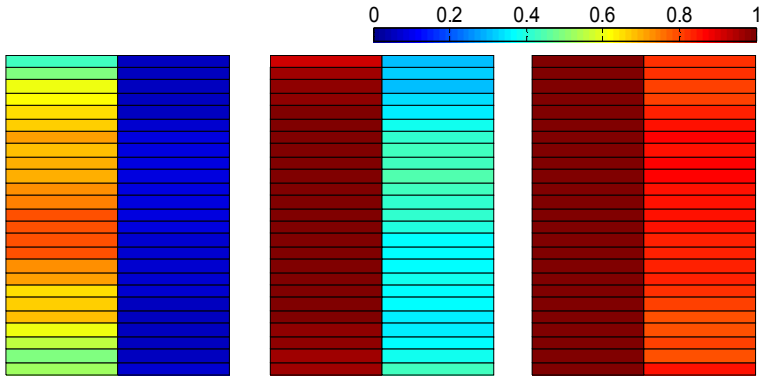

(a) AOA of 270˚

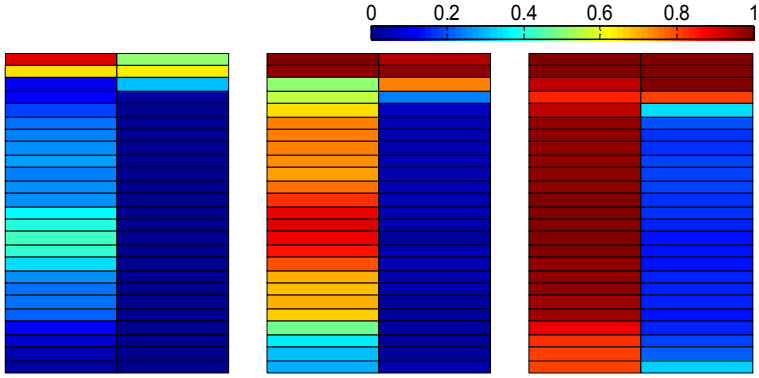

(b) AOA of 315˚

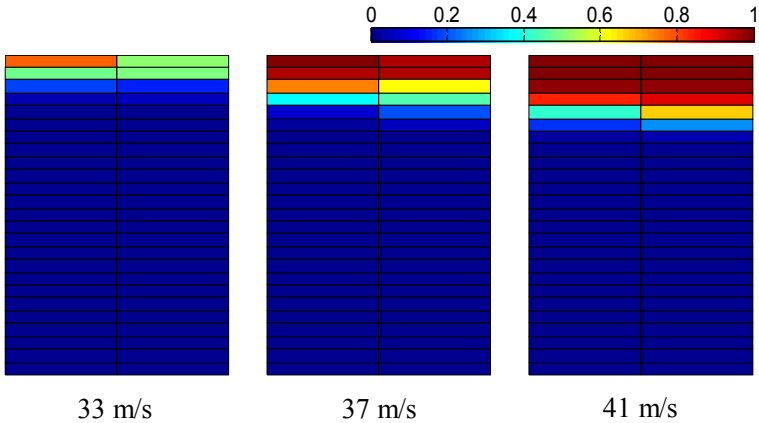

(c) AOA of 360˚

Figure 9 Claddings failure probabilities under wind speeds of 33, 37 and 41 m/s, and AOAs of 270˚, 315˚ and 360˚

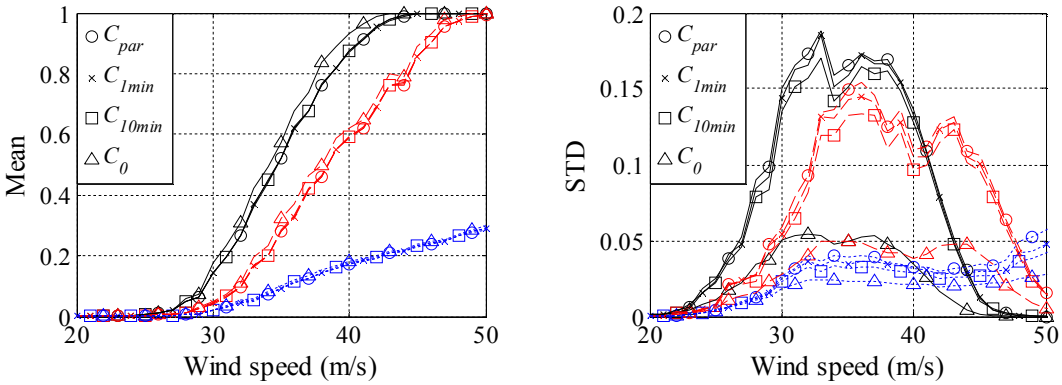

(a) Mean (b) STD

Figure 10 Damage ratios for various wind speeds and AOAs (black solid line: 270˚, red dash line: 315˚, blue dot line: 360˚)

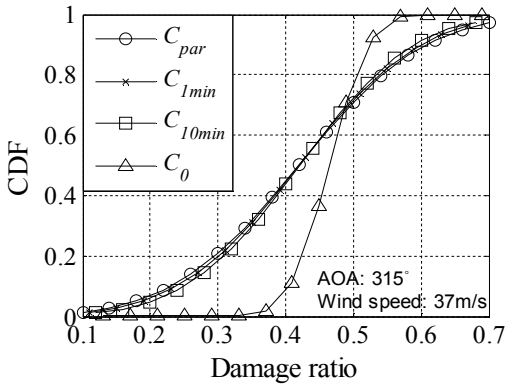

Figure 11 CDF of damage ratio under wind speed of 37 m/s and AOA of 315°

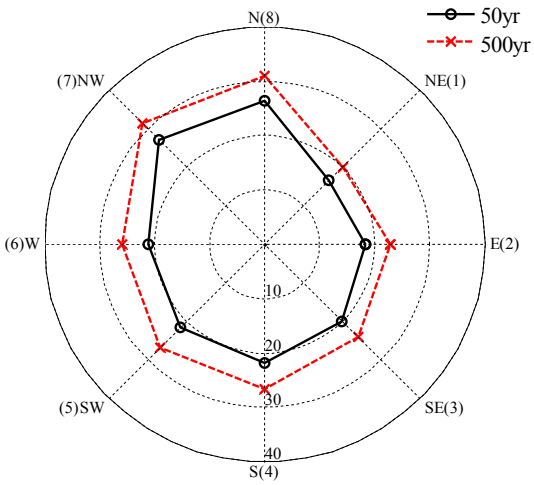

Figure 12 Extreme wind speeds for 50 and 500 –year return period (Unit: m/s)

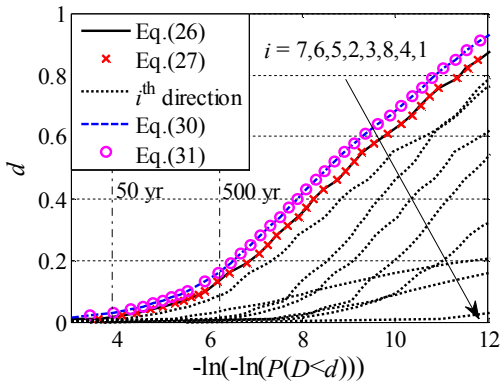

Figure 13 Estimations of roofing damage for various levels d

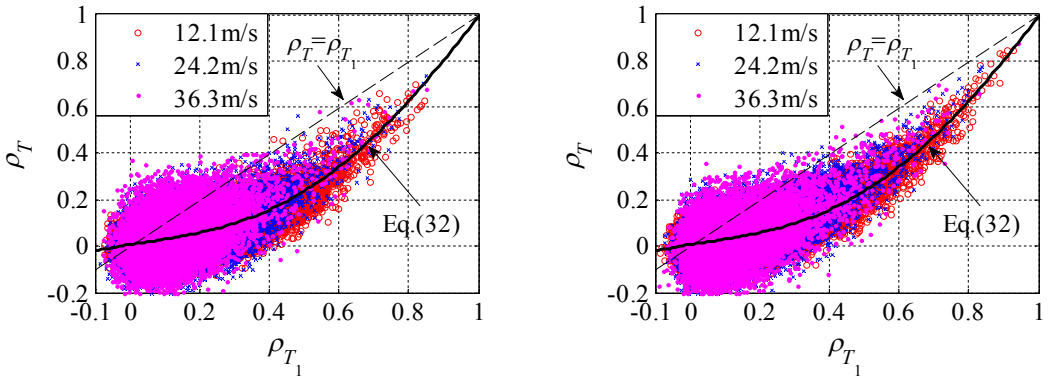

(a) FL27, 120˚, isolated (b) FL30, 130˚, surrounded

Figure 14 Correlation coefficients of peak pressure coefficients over T_1 and T

Table 1 Correlation coefficients among internal forces on selected screws (wind speed = 37 m/s and AOA = 315˚)

Screw	x2y2 (Cladding A)	x3y2 (Cladding A)	x4y1 (Cladding B)	x2y4 (Cladding C)	x2y3 (Cladding D)
x2y2 (Cladding A)	1				
x3y2 (Cladding A)	0.956 0.896 0.794	1			
x4y1 (Cladding B)	0.910 0.837 0.688	0.957 0.891 0.785	1		
x2y4 (Cladding C)	0.920 0.855 0.720	0.952 0.811 0.645	0.979 0.930 0.856	1	
x2y3 (Cladding D)	0.917 0.877 0.760	0.945 0.806 0.637	0.956 0.846 0.704	0.962 0.937 0.870	1

Note: Numbers represent C_{par}, C_{1min} and C_{10min} from top to bottom in a cell.